Three-Dimensional Reconstruction of an Erupting Filament with SDO and STEREO Observations

Ting Li, Jun Zhang, Yuzong Zhang, Shuhong Yang

Key Laboratory of Solar Activity, National Astronomical Observatories, Chinese Academy of Sciences, Beijing 100012, China

`[liting;zjun]@nao.cas.cn`

ABSTRACT

On 2010 August 1, a global solar event was launched involving almost the entire Earth−facing side of the Sun. This event mainly consisted of a C3.2 flare, a polar crown filament eruption and two Earth-directed coronal mass ejections (CMEs). The observations from the Solar Dynamics Observatory (SDO) and the Solar Terrestrial Relations Observatory (STEREO) showed that all the activities were coupled together, suggesting a global character of the magnetic eruption. We reconstruct the three-dimensional geometry of the polar crown filament using observations from three different viewpoints (STEREO A, B and SDO) for the first time. The filament undergoes two eruption processes. Firstly, the main body of the filament rises up, while it also moves towards the low-latitude region with a change in inclination by $\sim 48°$ and expands only in the altitudinal and latitudinal direction in the field of view of Atmospheric Imaging Assembly. We investigate the true velocities and accelerations of different locations along the filament, and find that the highest location always has the largest acceleration during this eruption process. During the late phase of the first eruption, part of the filament material separates from the eastern leg. This material displays a projectile motion and moves towards the west at a constant velocity of 141.8 km s^{-1}. This may imply that the polar crown filament consists of at least two groups of magnetic systems.

Subject headings: Sun: coronal mass ejections (CMEs) — Sun: filaments — Sun: flares

1. Introduction

The twin Solar Terrestrial Relations Observatory (STEREO; Kaiser et al. 2008; Howard et al. 2008) spacecraft provide simultaneous observations from two different points of view,

which enables us to reconstruct the three-dimensional (3D) geometry of coronal structures. After the launch of the STEREO mission, there have been many studies about the 3D reconstructions using data from the pair of Extreme UltraViolet Imagers (EUVI; see Wuelser et al. 2004). Feng et al. (2007) presented the first reconstruction of the 3D shape of coronal loops in an active region based on a triangulation technique. Aschwanden et al. (2008a, b, 2009) discussed the 3D geometry of coronal loops and determined the electron density and temperature of loops. Besides the coronal loops, the STEREO data have been used to reconstruct the active regions (Rodriguez et al. 2009; Wiegelmann & Inhester 2006), polar plumes (Curdt et al. 2008; Feng et al. 2009), polar coronal jets (Patsourakos et al. 2008) and coronal mass ejections (CMEs; Mierla et al. 2008; Timothy & Tappin 2008; Wood et al. 2009; Frazin et al. 2009).

Until now, there have been many studies about the nature of filament eruption and its role in disrupting the coronal magnetic fields (e.g., Zhang & Wang 2001; Zhang et al. 2001; Liu et al. 2007; Jiang et al. 2007; Liu et al. 2010; Guo et al. 2010a; Guo et al. 2010b). The dynamics of erupting filaments are very important to understand the associated physical mechanisms. However, filament velocity derived using traditional method has a disadvantage because it is only a projected velocity. Only recently, the true process of filament eruption could be properly judged by using the STEREO data (Li et al. 2010; Xu et al. 2010; Zapiór & Rudawy 2010; Gosain et al. 2009; Liewer et al. 2009; Bemporad 2011; Panasenco et al. 2011; Thompson 2011). Gissot et al. (2008) presented a fully automated optical-flow algorithm and estimated the height of an erupting filament from simultaneously obtained EUVI images. Thompson (2008) traced out a filament in 3D space and found a rotation of $\sim$ 140° from the original filament orientation. Bemporad (2009) found that the early filament expansion was anisotropic and occurred mainly on a plane parallel to the plane of the sky.

It is well known that the inner core of CME is made up of filament material (e.g., House et al. 1981). The slow rise of eruptive filaments linked to the streamer swelling is considered as the precursor of CMEs (Filippov & Koutchmy 2008). Thus an accurate measurement of filament motion is very useful in predicting the occurrence of a CME, as well as to constrain or construct the CME triggering mechanisms (Gopalswamy et al. 2006). Nevertheless, only several filaments have been reconstructed so far about their 3D shape and evolution using the STEREO data. The 3D physical picture of filament eruption is far from being completely understood. It is disadvantageous to reconstruct a 3D configuration of solar features by only using STEREO data because of the large separation angle between the two satellites. With the launch of the Solar Dynamics Observatory (SDO; Schwer et al. 2002), this would be much improved by using data of SDO and STEREO. In this work, we make the 3D reconstruction of a polar crown filament using observations from the three different viewpoints, and use a visualization method to display the reconstructed filament. Section

2 describes the instrumentation and observations. The 3D reconstruction technique and results are presented in Section 3. The eruptions of the polar crown filament are described in Sections 4, and the conclusions and discussion are given in Section 5.

2. Instrumentation and observations

The Atmospheric Imaging Assembly (AIA; Lemen et al. 2011) on the SDO has already provided a rich database since its launch in February 2010. AIA images are taken in 10 different wavelength bands, including one visible line, two ultraviolet and seven extreme ultraviolet (EUV) channels. It provides full-disk images, covering a wide range of temperatures, with high cadence (up to $12-24$ s) and spatial resolution (0.6 arcsec pixel^{-1}). The full-disk longitudinal magnetic field from the Helioseismic and Magnetic Imager (HMI; Schou et al. 2011) aboard SDO is available now, with high cadence (~ 45 s) and spatial resolution (0.5 arcsec pixel^{-1}).

The Sun Earth Connection Coronal and Heliospheric Investigation (SECCHI; Howard et al. 2008) imaging package on each spacecraft of the STEREO consists of the following five telescopes: the EUVI imager, inner (COR1) and outer (COR2) coronagraphs, and inner (HI1) and outer (HI2) heliospheric imagers. EUVI images are taken at four wavelengths centered at 304 Å, 171 Å, 195 Å, and 284 Å with time cadences of 10, 2.5, 10, and 20 minutes, respectively, for the data used here. COR1 has a field of view (FOV) from 1.4 to 4 R_{sun} and COR2 from 2.5 to 15 R_{sun}.

On 2010 August 1, a spectacular solar event was launched involving almost the entire Earth−facing side of the Sun. At about 05:00 UT, a large-scale ($\sim 750,000$ km) polar crown filament stretching across the solar northern hemisphere began to rise slowly. Then a C3.2 flare occurred at 07:24 UT in active region 11092, with a distance of $\sim 430,000$ km from the long filament. At about 07:50 UT, an Earth-directed CME (CME front "a" in Figure 1) was observed by the COR1 aboard STEREO A. The average velocity of the first CME in the FOV of COR1 was about 624 km s^{-1}, and the angular width was $\sim 144°$. At about 09:00 UT, another Earth-directed CME occurred and the eruptive filament was the bright core of the second CME (right panels in Figure 1). The second CME had an average velocity of 260 km s^{-1} in the FOV of COR1, and its angular width was about 83°. Based on the Michelson Doppler Imager (MDI) magnetograms, we carried out the global reconstruction of 3D magnetic-field structure under the potential-field assumption. The boundary element method (BEM) was used in the extrapolation (Yan & Sakurai 2000; Wang et al. 2002; Zhang et al. 2007). We found that there were two groups of magnetic structures overlying the filament (the large-scale magnetic structures denoted by character "a" and the smaller

magnetic structures beneath the large-scale ones denoted by "b" in top panels of Figure 1).

Here, we concentrate on the eruption process of the large polar crown filament. The filament eruption was recorded in all AIA channels, and the 304 Å images with a time cadence of 12 s were used. The eruption was also observed as a limb event at 304 Å by the two EUVIs aboard STEREO. The pixel size of the EUVI image on the solar disk was 1.6 arcsec, and the time cadence for 304 Å images was 10 minutes.

3. Reconstruction technique and results

For the first time, we combine data from SDO and STEREO to reconstruct the erupting filament. The angle of separation between STEREO A and B during our observations is around $149°.6$. It is difficult to define the same feature in EUVI A and B images because of the large separation angle. The separation angle between STEREO A and SDO is $78°.8$, and that between STEREO B and SDO $70°.8$. So observations from the three different viewpoints are used here to derive the 3D erupting process of the polar crown filament. The western part of the filament was observed clearly by STEREO A and SDO, and thus we reconstruct the western part by using data from STEREO A and SDO (Figures 2 and 3). Similarly, the eastern part is reconstructed by using observations of STEREO B and SDO (Figures 2 and 4).

In order to reconstruct the 3D shape of the eruptive filament, we use a routine called SCC_MEASURE (developed by W. Thompson), which is available in the STEREO package of the Solar Software library. The routine uses triangulation to determine the 3D coordinate of the tiepointed feature. It is a widget based application that allows the user to locate (and select with a cursor) the same feature in two images from different views. This routine makes use of an approximate "epipolar constraint" in locating the same feature in both images (Inhester 2006). The two observer positions and any object point to be reconstructed exactly define a plane, which is known as an epipolar plane. By definition, epipolar planes are projected on both observers images as lines and these lines are called the epipolar lines. Once we identify a feature in one image, it is possible to determine the projection of the epipolar plane (i.e., epipolar line) passing the same feature in the second image. After selecting the same feature in both images, the 3D coordinates are then determined as longitude, latitude, and radial distance from the center of the Sun.

It must be mentioned that there exists a limiting factor in reconstructing filaments, because the reconstruction technique relies on the ability to identify the same feature in two images from different views. In fact, much of the corona is optically thin, so the emission

at each pixel may be the result of a line-of-sight integration effect. Moreover, features may appear different from different angles due to the projection effect. In order to reduce the uncertainty, we examine the movies of filament eruption carefully and determine the features according to their evolution. We also use the bright or dark patterns in adjacent areas to identify the features. As seen in Figure 7, the measurement is repeated by two researchers, and each researcher measures twice. The standard deviations in the four sets of measurements are considered as the realistic uncertainties. The average values in the four sets of measurements are thought to be the real values.

About four hours after the onset of the rise, the filament lifted up to a high altitude above the solar surface and it became blurry because of the steep radial intensity gradient. So we reconstruct the 3D shape and evolution of the eruptive filament between 05:06 and 09:26 UT. We choose the top edge, the main-body line and the bottom edge as three baselines of the filament. For the western part of the filament, 20 pairs of points are placed along each baseline in the images of STEREO A and SDO. For the eastern part, 16 pairs of points are placed along each baseline in the images of STEREO B and SDO. Therefore, 36 pairs of points are placed along each baseline for the entire filament. We interpolate 500 points by using a cubic spline along each baseline among the selected points to smooth the baseline. Then we simply fill in the enclosed region between any two baselines with 1000 triangular elements to produce the extended regions. Using this visualization method, we can display the reconstructed filament seen from any visual angle.

The reconstructed filament seen from the SDO viewpoint at three different times is shown in Figure 2. The filament began to gradually lift up at 05:06 UT. It spanned a longitude range of about $42°.3$ (from $3°.3$ E to $39°.0$ W measured from the central meridian) and a latitude range of about $26°.0$ (from $20°.6$ N to $46°.6$ N). The filament had the initial length of 1.07 R_{sun}, and the highest part at that time was approximately at 1.15 R_{sun}. Then it moved towards the north pole as seen from the SDO, and rose to a height of 1.31 R_{sun} at 07:36 UT. At about 09:00 UT, the western part of the filament broke up and then it was ejected from the Sun (bottom panels).

From the STEREO A perspective (Figure 3), the evolution of the western part is displayed clearly. The filament has two main endpoints at its west, composing a reverse−Y shape. The distance between the two ends of the reverse−Y shape is 197.4 Mm. The distance between the northern (southern) end and the intersection is 109.2 Mm (135.8 Mm). The northern endpoint could not be seen clearly before the rapid ascent of the filament (top panels). With the ascent of the filament, the reverse−Y structure is obviously seen and the endpoint brightenings are observed simultaneously (bottom panels). Strong and relatively concentrated brightenings occur at the northern endpoint, while weaker and more dispersed

EUV enhancements are seen along the multiple, curved threads at its southern endpoint. At 08:36 UT, the strands of the filament anchoring the two ends are separated from each other. Then the strands anchoring the northern end is disconnected, and the area of brightenings at the northern endpoint expanded towards the northeast. The barbs of the filament could be observed clearly from the STEREO B perspective (denoted by white circles in Figure 4). At 05:06 UT, all the barbs are tightly anchored in the photosphere. Then the barbs are elongated and finally cut off from the solar surface in sequence due to the rise of the eastern part.

We reconstruct the eastern part of the filament by using data of STEREO B and SDO, and reconstruct the western part using data of STEREO A and SDO. For the eastern part, the STEREO A viewpoint is the third view to confirm the result. The eastern part of the reconstructed filament seen from STEREO A is similar to the observed eastern part (Figure 3). Similarly, the STEREO B viewpoint is the third view to confirm the result for the western part. The reconstructed western part seen from STEREO B is similar to the observed western part (Figure 4). These imply that our reconstruction results are reliable to some extent.

We display the reconstructed filament seen from three different points of view in Figure 5. The left panels show the results seen from the top of the filament center, which is the central location of the main body at 05:06 UT on the solar surface (denoted by plus signs in panels (a) and (e); with a longitude of 12°.1 W and a latitude of 39°.4 N). With the radial distance from the center of the Sun increasing, the latitude of the filament decreases gradually. The longitude of the filament remains approximately invariable. This implies that the eruption is non-radial. The angle between the radial direction (lines in panels (d)−(f); connecting the filament center at 05:06 UT with the solar center) and the line connecting the highest part with the filament center at 05:06 UT is considered as the inclination of the filament (panel (e)). The filament is initially inclined northward with an inclination of $\sim 40°$. Then it moves towards the low-latitude region and is inclined southward with an inclination of $\sim 8°$ at 09:26 UT. Seen from the north pole, the velocity of the filament has a large Earth−directed component (panels (g)−(i)). This is consistent with the Earth−directed CME associated with the filament eruption (right panels in Figure 1).

4. Eruptions of the filament

4.1. First eruption of the filament

In order to analyze the filament eruption in detail, we investigate the true velocities and accelerations of different sites along the filament. Eleven points (points "1" to "11" in Figure 6) are selected along the filament body at each time. Points "1" to "4" are defined using data of SDO and STEREO B, and points "5" to "11" are selected in SDO and STEREO A images. Due to motions of the material, it is difficult to define the same feature during a period. So we examine the movies of the filament eruption carefully, and select four specific points ("1", "5", "10" and "11") according to their continuous evolution. Points "1" and "11" are near the two ends of the filament. Points "5" and "10" are placed at the top and bottom corners, respectively. Then we place other points equally between each two specific neighboring points according to SDO/AIA images. Thus all the 11 points along the main body are defined at each time.

Because the velocity-location plots of the 11 points at different times are similar, we only display the plots at three times (Figures 7(a) and (b)). Point "5" at the top corner of the filament is always the highest among the 11 points. It also has the largest velocity and acceleration at any time. Moreover, the true heights, velocities and accelerations of the highest point between 04:56 UT and 09:36 UT are presented (Figure 7(c)). The height of the filament increased by 0.72 R_{sun} over four hours. There is some evidence for a slight, slow rise before the fast eruption. Before 07:06 UT, the filament lifted up gradually; the velocity and acceleration were less than 13.8 km s^{-1} and 3.0 m s^{-2}, respectively. Then it ascended more rapidly and reached a velocity of 144.8 km s^{-1} at 09:26 UT. Arrows in Figure 7(c) show the time of the C3.2 flare start (07:24 UT) and peak (08:56 UT). About 30 minutes before the flare onset, the acceleration of the highest point began to increase and reached a value of 9.2 m s^{-2} at 07:36 UT. Then it decreased to 5.2 m s^{-2} at 07:56 UT and increased to 41.2 m s^{-2} at 09:16 UT afterwards. When the velocity of the filament continuously increased to about 90 km s^{-1} at 09:06 UT, the associated CME was clearly observed in STEREO A/COR1 images. At this time, the velocity of the CME was 163 km s^{-1} (Figure 7(d)), which is more than the velocity of the filament by a factor as large as 1.8. Then the velocity of the second CME increased to 762 km s^{-1} at 13:18 UT in the FOV of COR2 (Figure 7(d)).

We also investigate the variations of the longitudes and latitudes for the reconstructed features during the fast-eruptive phase (between 07:06 and 09:26 UT). As seen in Figure 8, the longitudes of points "2" to "4" at the eastern leg show a decrease of $\sim 7°$, while points "6" to "9" at the western leg show an increase in longitude of about 12°. The latitudes of all the points except "9" are seen to decrease by $\sim 5°$. The measurement is repeated four times,

and the corresponding errors in longitude and latitude are about $0°.6$ and $0°.3$, respectively. Similar to the analysis of Joshi & Srivastava (2011), our analysis indicates that the filament experiences a twist in a counterclockwise direction.

In the process of the filament eruption, the EUV enhancements at the endpoints are observed clearly (top panel in Figure 9). At about 07:20 UT, the initial brightenings occurred at the eastern endpoints. At 08:20 UT, the brightenings at the western endpoints were observed. Comparison with the magnetograms shows that the western (eastern) ends of the filament are rooted in negative- (positive-) polarity fields (Figure 9). The magnetic polarity of the ends determines the direction of the axial field component of the filament. According to the empirical rule of Martin (1998), if the barbs point forward and to the right (left), then the axial field points to the right (left) when viewed from the positive-polarity side of the polarity inversion line, and the filament has "left-handed" ("right-handed") chirality. Therefore, the filament is left-handed.

4.2. Second eruption of the filament

At the late phase of the first eruption ($\sim$ 09:30 UT), the eastern leg of the erupting filament obviously started to expand. Then partial material from the filament separated from the eastern leg (see rectangle "1" in Figure 10(b)). The separated material gradually diffused towards the west and the orientation of the separated material became mainly northeast-southwest at 10:16 UT from the longitudinal direction at 09:51 UT (Figure 10(b)). This material displayed a projectile motion and moved along the filament channel in AIA images (Figure 10(a)). The material became invisible at 11:25 UT when it moved to the west limb.

In order to follow the motion of the material in detail, we select the slice (line A-B in Figure 10) along which the material moves from the running ratio 304 Å images. As seen in the running ratio stack plot (Figure 10(c)), the material moves at a nearly constant speed. The velocities of two clear structures are about 145.2 km s^{-1} and 138.3 km s^{-1}. In the first eruption, the main body of the filament lifted up and was accelerated (Figure 7(c)). In the second eruption, partial material of the eastern leg displayed a projectile motion toward the west and the velocity remained constant.

5. Conclusions and discussion

On 2010 August 1, a C3.2 flare, a polar crown filament eruption and two Earth-directed CMEs were coupled together, indicating the global character of solar activity (Wang et al.

2007; Zhukov & Veselovsky 2007; Zhou et al. 2007). Schrijver & Title (2011) analyzed a series of events occurring on 2010 August 1-2, and concluded that all substantial coronal activities were initiated from a connected network of large-scale separators, separatrices, and quasi-separatrix layers. Also they found that the magnetic field lines emanating from the flare region slid over a quasi-separatrix layer connecting the polar crown filament.

For the first time, we reconstruct the polar crown filament using observations from three different viewpoints (STEREO A, B and SDO). The initial length of the filament was 1.07 R_{sun}, and the highest part was approximately at 1.15 R_{sun}. Three hours after the initial ascent, it rose to a height of 1.47 R_{sun} and the length increased to 1.75 R_{sun}, about 1.6 times as long as the initial length. Two western endpoints and a partial spine of the filament compose a reverse−Y structure. During the eruption, the barbs are elongated and finally cut off from the solar surface in sequence. AIA observations show that the slow-rise phase of the filament lasts about two hours, and the velocity and acceleration at the highest location are less than 13.8 km s^{-1} and 3.0 m s^{-2}, respectively. Then it ascends more rapidly and reaches a velocity of 144.8 km s^{-1} at 09:26 UT and an acceleration of 41.2 m s^{-2} at 09:16 UT. The highest location always has the largest acceleration, implying that the location bears the largest force during the eruption process. This result is different from a former study (Li et al. 2010) that the location bearing the largest force varies during a filament eruption process.

The reconstructed filament is processed with a visualization method and we can view it from any visual angle. The reconstructed western part of the filament gained with STEREO A and SDO data seen from the third viewpoint (STEREO B) is similar to the observations. This indicates that our reconstruction results are reliable to some extent. Seen from the north pole, the velocity of the filament has a large Earth−directed component. This is consistent with the Earth−directed CME accompanying the eruptive filament. The filament moves towards the low-latitude region, with an inclination change of ∼ 48° with respect to the radial direction in the FOV of AIA. The filament expands only in altitude and in the latitudinal direction, similar to the conclusion made by Bemporad (2009), who found that the radial and latitudinal expansions of the filament are much larger than the longitudinal ones and suggested that the filament can be approximated as a 2D "ribbon-like" feature, instead of a 3D twisted flux tube.

In addition, at the late phase of the first eruption, partial material separates from the eastern leg. This material displays a projectile motion, and moves towards the west at a constant velocity of 141.8 km s^{-1}. To our knowledge, this phenomenon has never been reported before. The velocity of the second eruption remains approximately constant, while the velocity of the first eruption increases with time, which indicates that their eruption

mechanisms are different. Hirose et al. (2001) concluded that the filament with helical fields accelerate upward in a round-shaped expanding field structure forming a CME containing the eruptive filament. The first eruption corresponds to the rise of helical magnetic fields of the filament (Jing et al. 2004; Sterling et al. 2007; DeVore & Antiochos 2008), and the second eruption is the motion of filament material along the magnetic system due to unequal magnetic pressure. The observations may imply that the polar crown filament consists of at least two groups of magnetic systems.

REFERENCES

Aschwanden, M. J., Nitta, N. V., Wuelser, J.-P., & Lemen, J. R. 2008a, ApJ, 680, 1477

Aschwanden, M. J., Wuelser, J.-P., Nitta, N. V., & Lemen, J. R. 2008b, ApJ, 679, 827

Aschwanden, M. J., Wuelser, J.-P., Nitta, N. V., Lemen, J. R., & Sandman, A. 2009, ApJ, 695, 12

Bemporad, A. 2009, ApJ, 701, 298

Bemporad, A. 2011, J. Atmos. Sol.-Terr. Phys., 73, 1117

Curdt, W., Wilhelm, K., Feng, L., & Kamio, S. 2008, A&A, 481, L61

DeVore, C. R., & Antiochos, S. K. 2008, ApJ, 680, 740

Feng, L., Inhester, B., Solanki, S. K., Wiegelmann, T., Podlipnik, B., Howard, R. A., & Wuelser, J.-P. 2007, ApJ, 671, L205

Feng, L., et al. 2009, ApJ, 700, 292

Filippov, B., & Koutchmy, S. 2008, Ann. Geophys., 26, 3025

Frazin, R. A., Jacob, M., Manchester, W. B., Morgan, H., & Wakin, M. B. 2009, ApJ, 695, 636

Gissot, S.F., Hochedez, J.-F., Chainais, P., & Antoine, J.-P. 2008, Sol. Phys., 252, 397

Gopalswamy, N., Mikić, Z., Maia, D., Alexander, D., Cremades, H., Kaufmann, P., Tripathi, D., & Wang, Y.-M. 2006, Space Sci. Rev., 123, 303

Gosain, S., Schmieder, B., Venkatakrishnan, P., Chandra, R., & Artzner, G. 2009, Sol. Phys., 259, 13

Guo, J., Liu, Y., Zhang, H., Deng, Y., Lin, J., & Su, J. 2010, ApJ, 711, 1057

Guo, Y., Schmieder, B., Démoulin, P., Wiegelmann, T., Aulanier, G., Török, T., & Bommier, V. 2010, ApJ, 714, 343

Hirose, S., Uchida, Y., Uemure, S., Yamaguchi, T., & Cable, S. B. 2001, ApJ, 551, 586

House, L. L., Wagner, W. J., Hildner, E., Sawyer, C., & Schmidt, H. U. 1981, ApJ, 244, L117

Howard, R. A., et al. 2008, Space Sci. Rev., 136, 67

Inhester, B. 2006, arXiv: astro-ph/0612649

Jiang, Y., Yang, L., Li, K., & Shen, Y. 2007, ApJ, 667, L105

Jing, J., Yurchyshyn, V. B., Yang, G., Xu, Y., & Wang, H. M. 2004, ApJ, 614, 1054

Joshi, A. D., & Srivastava, N. 2011, ApJ, 730, 104

Kaiser, M. L., Kucera, T. A., Davila, J. M., St. Cyr, O. C., Guhathakurta, M., & Christian, E. 2008, Space Sci. Rev., 136, 5

Lemen, J. R., et al. 2011, Sol. Phys., in press

Li, T., Zhang, J., Zhao, H., & Yang, S. 2010, ApJ, 720, 144

Liewer, P. C., de Jong, E. M., Hall, J. R., Howard, R. A., Thompson, W. T., Culhane, J. L., Bone, L., & van Driel-Gesztelyi, L. 2009, Sol. Phys., 256, 57

Liu, R., Alexander, D., & Gilbert, H. R. 2007, ApJ, 661, 1260

Liu, R., Liu, C., Wang, S., Deng, N., & Wang, H. 2010, ApJ, 725, L84

Martin, S. F. 1998, Sol. Phys., 182, 107

Mierla, M., et al. 2008, Sol. Phys., 252, 385

Panasenco, O., Martin, S., Joshi, A. D., & Srivastava, N. 2011, J. Atmos. Sol.-Terr. Phys., 73, 1129

Patsourakos, S., Pariat, E., Vourlidas, A., Antiochos, S. K., & Wuelser, J. P. 2008, ApJ, 680, L73

Rodriguez, L., Zhukov, A. N., Gissot, S., & Mierla, M. 2009, Sol. Phys., 256, 41

Schou, J., et al. 2011, Sol. Phys., submitted

Schrijver, C. J., & Title, A. M. 2011, Journal of Geophysical Research, 116, 4108

Schwer, K., Lilly, R. B., Thompson, B. J., & Brewer, D. A. 2002, AGU Fall Meeting Abstracts, C1

Sterling, A. C., Harra, L. K., & Moore, R. L. 2007, ApJ, 669, 1359

Thompson, W. T. 2008, in American Geophysical Union, Fall Meeting 2008, 3D Reconstruction of an Erupting Prominence (Washington, DC: American Geophysical Union)

Thompson, W. T. 2011, J. Atmos. Sol.-Terr. Phys., 73, 1138

Timothy, A. H., & Tappin, S. J. 2008, Sol. Phys., 252, 373

Wang, J., Zhang, Y., Zhou, G., Harra, L. K., Williams, D. R., & Jiang, Y. 2007, Sol. Phys., 244, 75

Wang, T., Yan, Y., & Wang, J. 2002, ApJ. 572, 580

Wiegelmann, T., & Inhester, B. 2006, Sol. Phys., 236, 25

Wood, B. E., Howard, R. A., Thernisien, A., Plunkett, S. P., & Socker, D. G. 2009, Sol. Phys., 259, 163

Wuelser, J. P., et al. 2004, Proc. SPIE, 5171, 111

Xu, Y., Jing, J., & Wang, H. 2010, Sol. Phys., 264, 81

Yan, Y., & Sakurai, T. 2000, Sol. Phys., 195, 89

Zapiór, M., & Rudawy, P. 2010, Sol. Phys., 267, 95

Zhang, J., & Wang, J. 2001, ApJ, 554, 474

Zhang, J., Wang, J., Deng, Y., & Wu, D. 2001, ApJ, 548, L99

Zhang, Y., Wang, J., Attrill, G. D. R., Harra, L. K., Yang, Z., & He, X. 2007, Sol. Phys., 241, 329

Zhou, G., Wang, J., Wang, Y., & Zhang, Y. 2007, Solar Phys., 244, 13

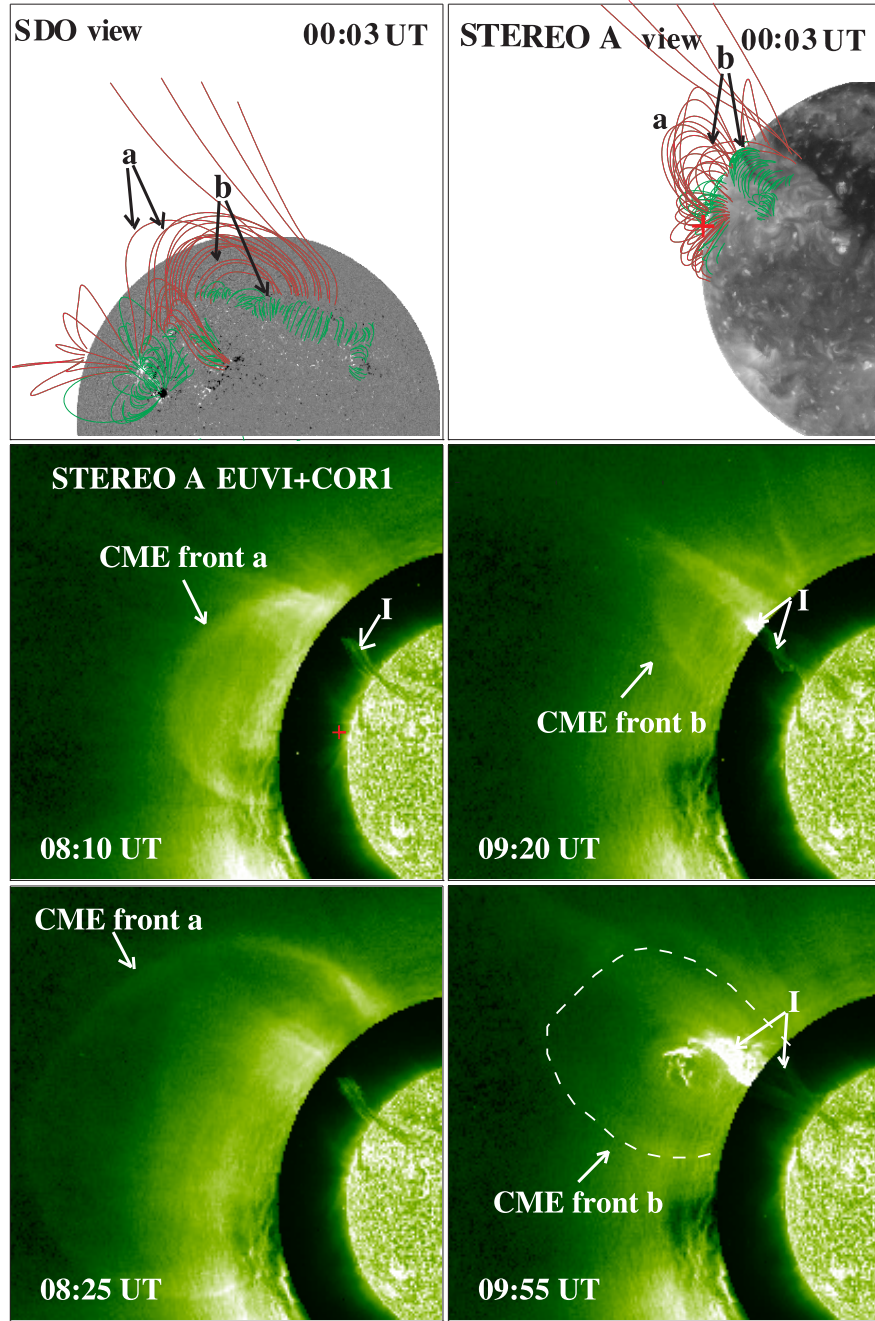Zhukov, A. N., & Veselovsky, I. S. 2007, ApJ, 664, L131

_____

Fig. 1.— Extrapolated coronal magnetic field lines seen from the SDO (top left) and STEREO A (top right) perspectives at 00:03 UT on 2010 August 1 and composite images (middle and bottom panels) of STEREO-A COR1 and EUVI 304 Å. The backgrounds in the top panels are the MDI line-of-sight magnetogram at 00:03 UT and the STEREO A 195 Å image at 00:05 UT, respectively. Characters "a" and "b" denote the large-scale and small magnetic structures. Red and green curves represent high and low magnetic lines. Arrows "I" indicate the filament material. The plus signs denote the flare position.
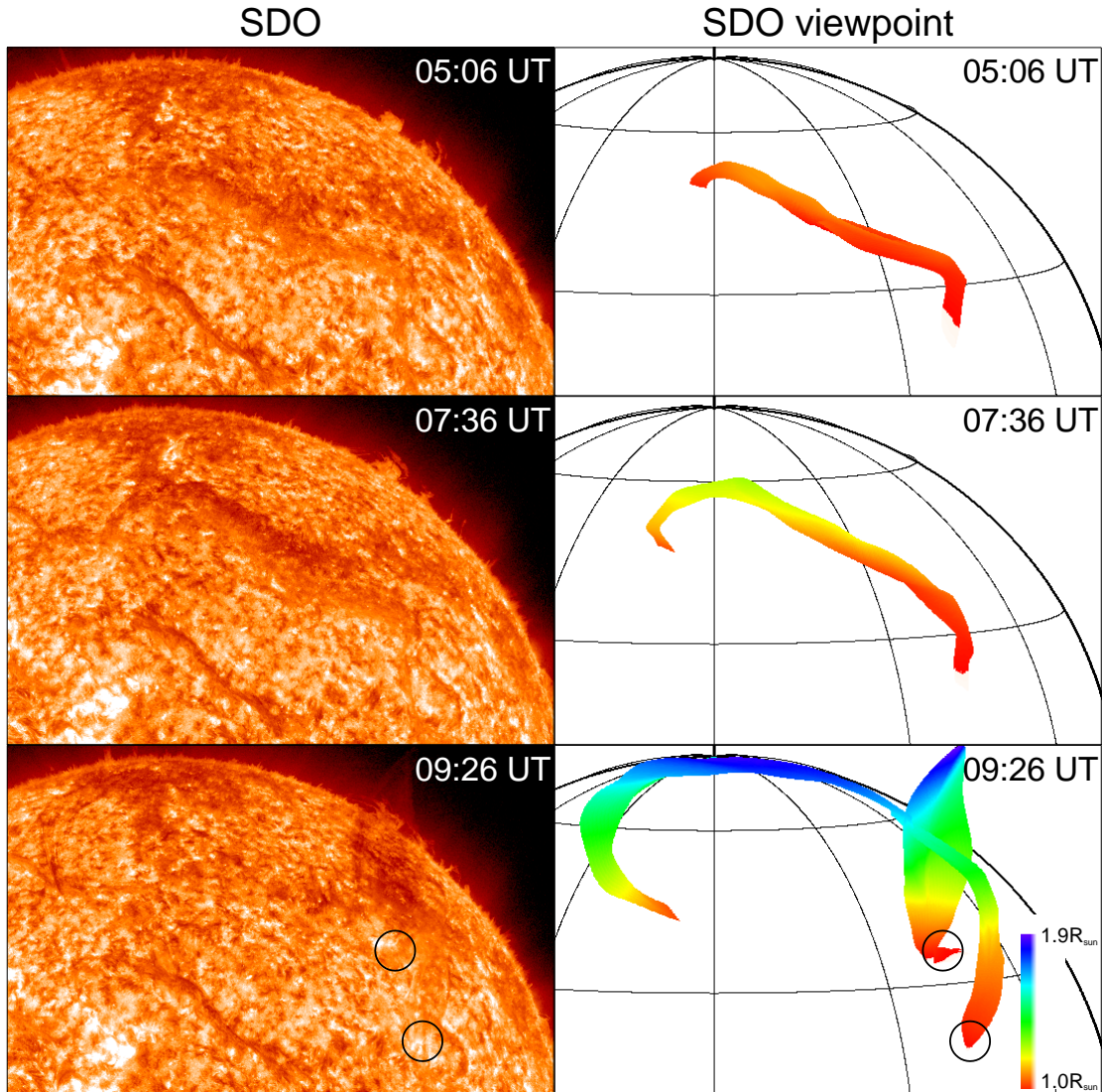
Fig. 2.— Reconstructed filament seen from the SDO viewpoint. Left: a series of SDO/AIA 304 Å observed images showing the evolution of the filament. Right: a series of reconstructed images seen from the SDO viewpoint showing the eruption process of the filament. The black circles denote the western endpoints of the filament.
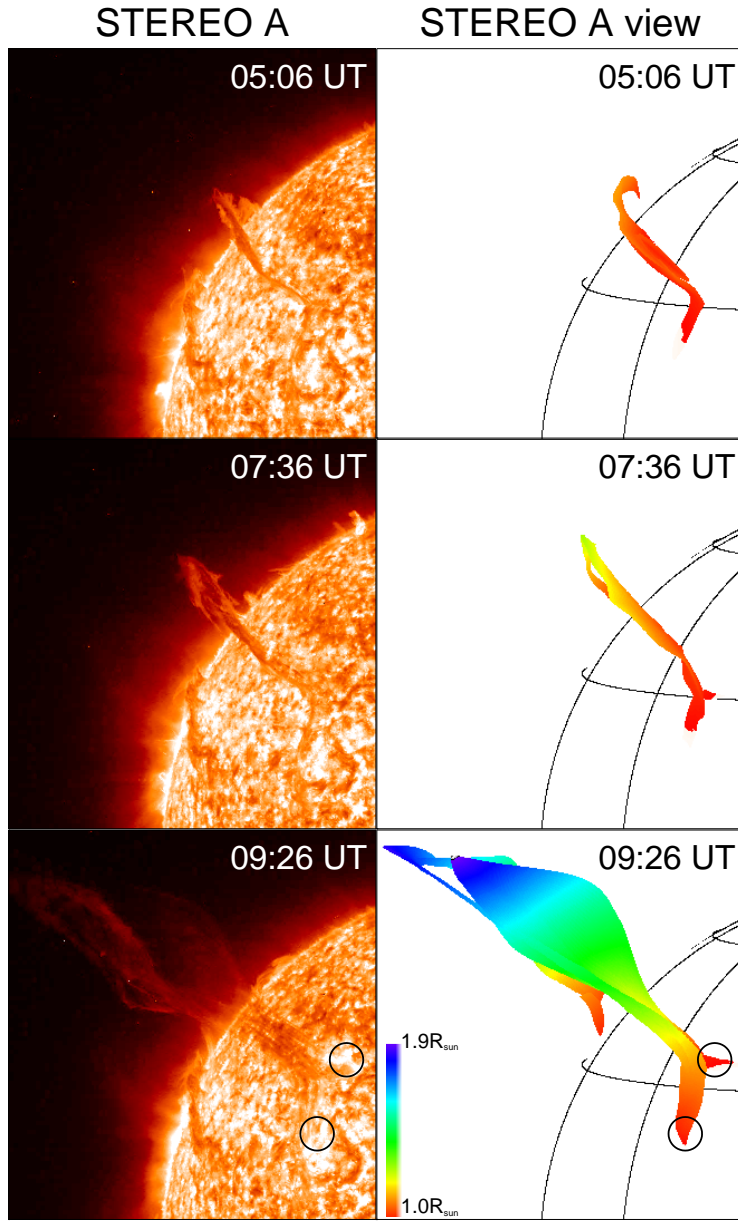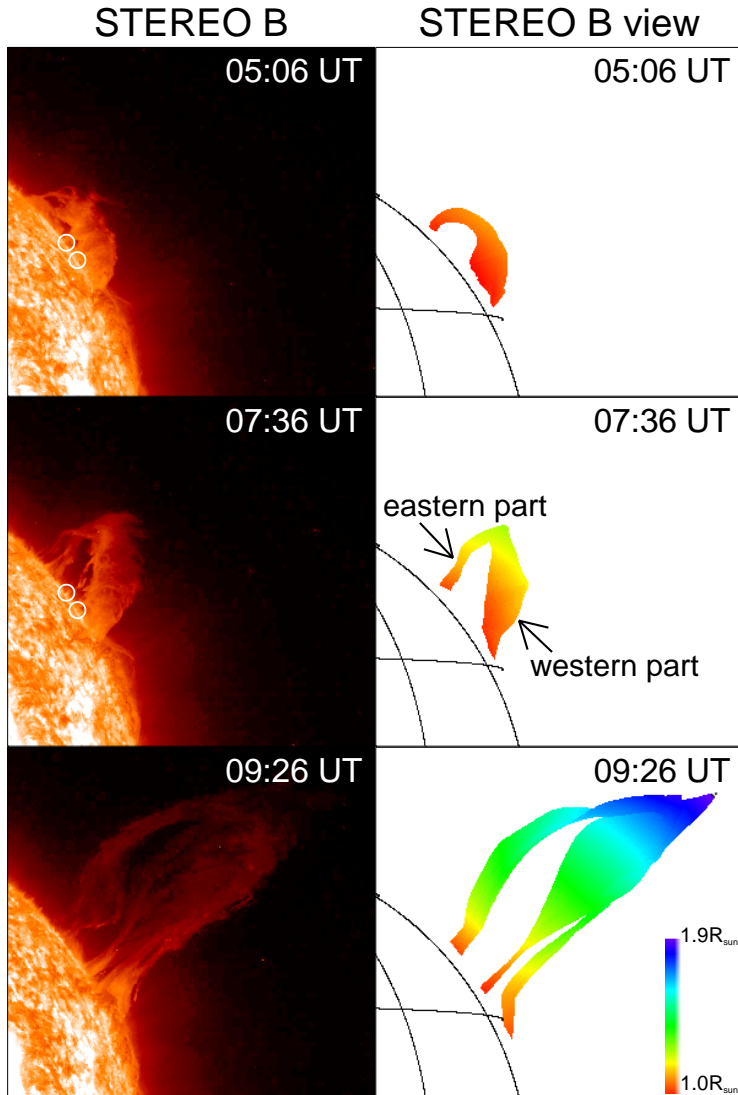
Fig. 3.— Comparison of the observed filament (left panels) and the reconstructed filament (right panels) seen from the STEREO A view. The black circles denote the western endpoints of the filament.

Fig. 4.— Comparison of the observed filament (left panels) and the reconstructed filament (right panels) seen from the STEREO B view. The white circles denote the barbs of the filament.
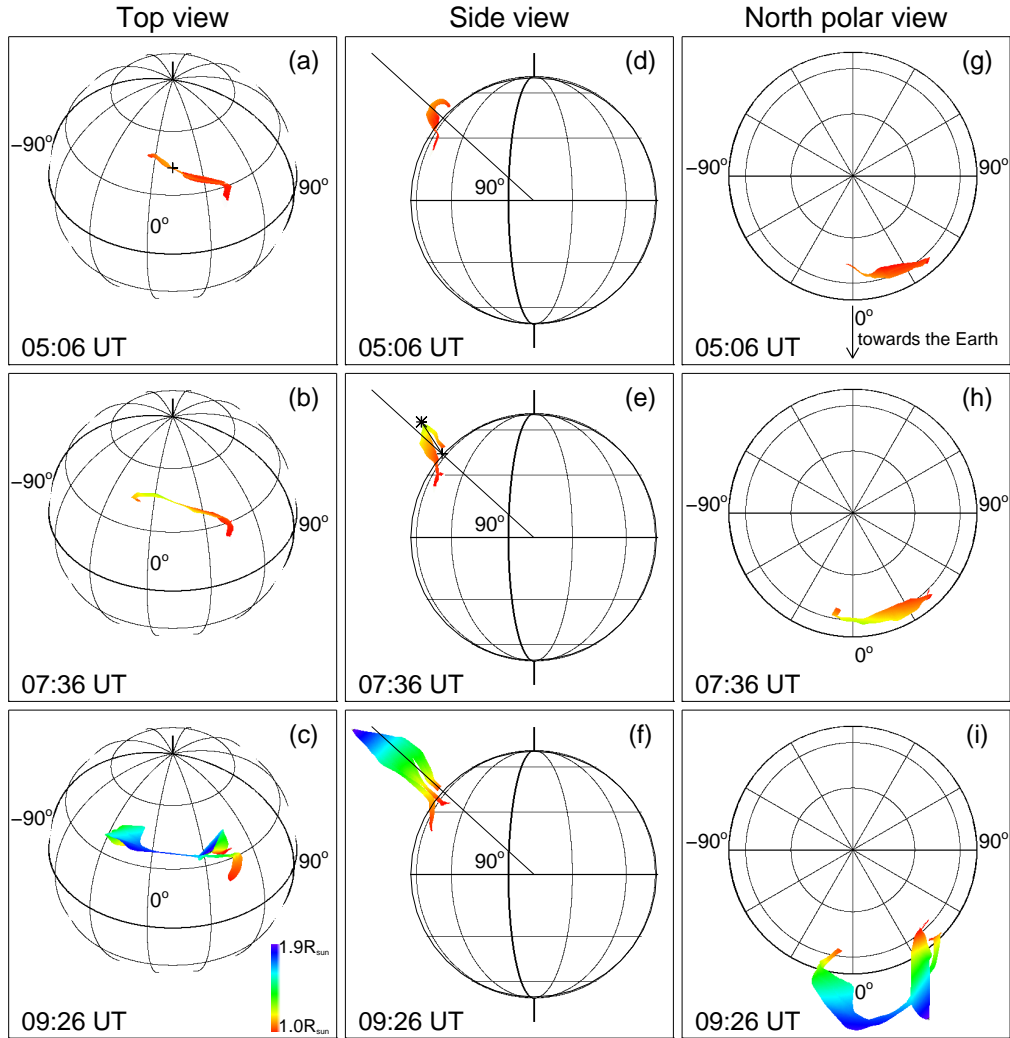
Fig. 5.— Evolution of the reconstructed filament seen from the top view (left panels), the side view (middle panels) and the north polar view (right panels). In the heliographic coordinate system, the top view of the filament has a longitude of 12° and a latitude of 39°, and the side view has a longitude of 102° and a latitude of 0°.
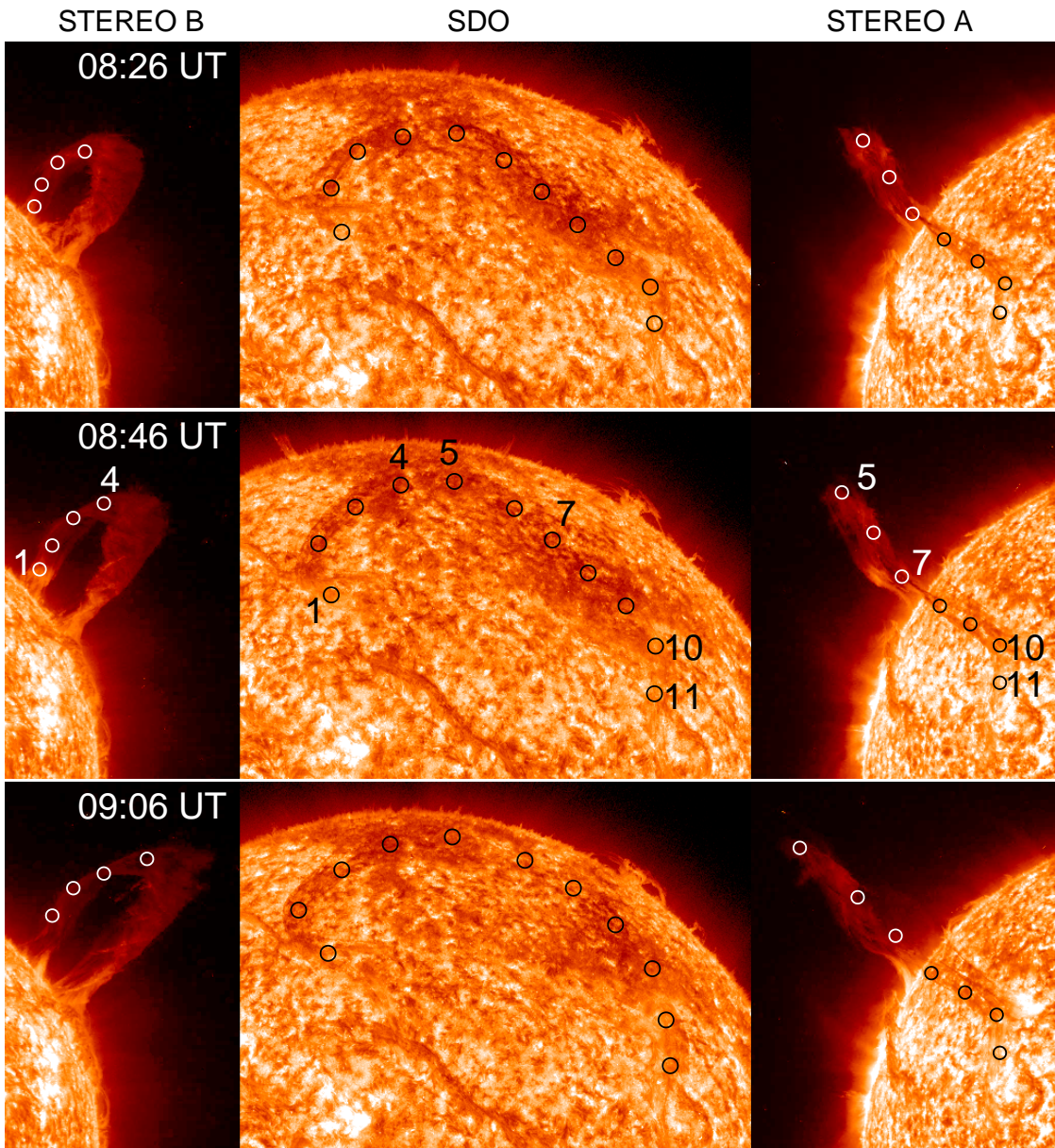
Fig. 6.— Locations of 11 points selected in SDO and STEREO images. The circles denote the 11 points along the filament.
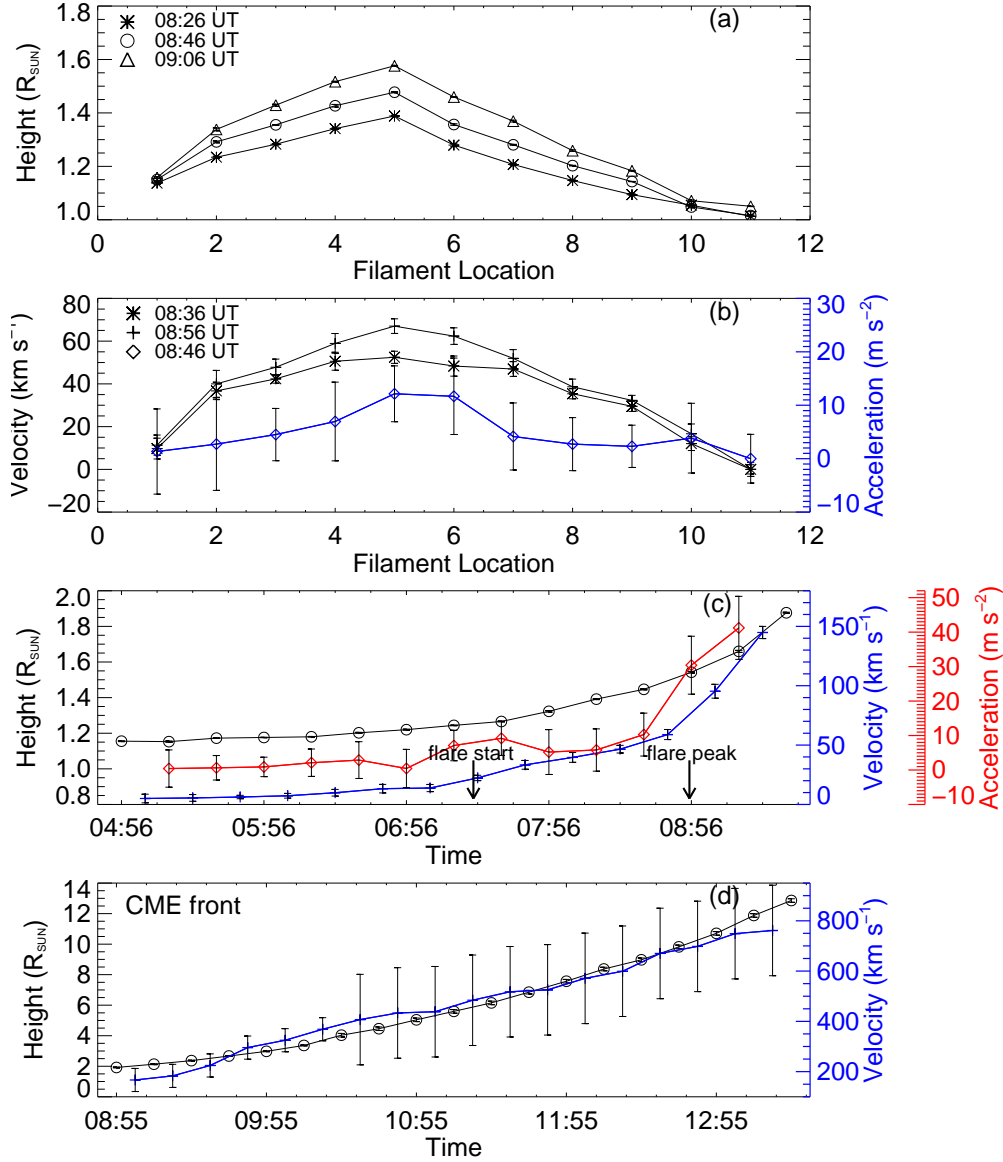
Fig. 7.— (a): True height-location plots of the 11 points (points "1" to "11" in Figure 6) at three different times. (b): Velocity-location and acceleration-location plots of the 11 points. (c): True height-time, velocity-time and acceleration-time plots of the highest point between 04:56 UT and 09:36 UT. (d): Projected height-time and velocity-time plots of the associated CME measured in STEREO A/COR1 and COR2 images.
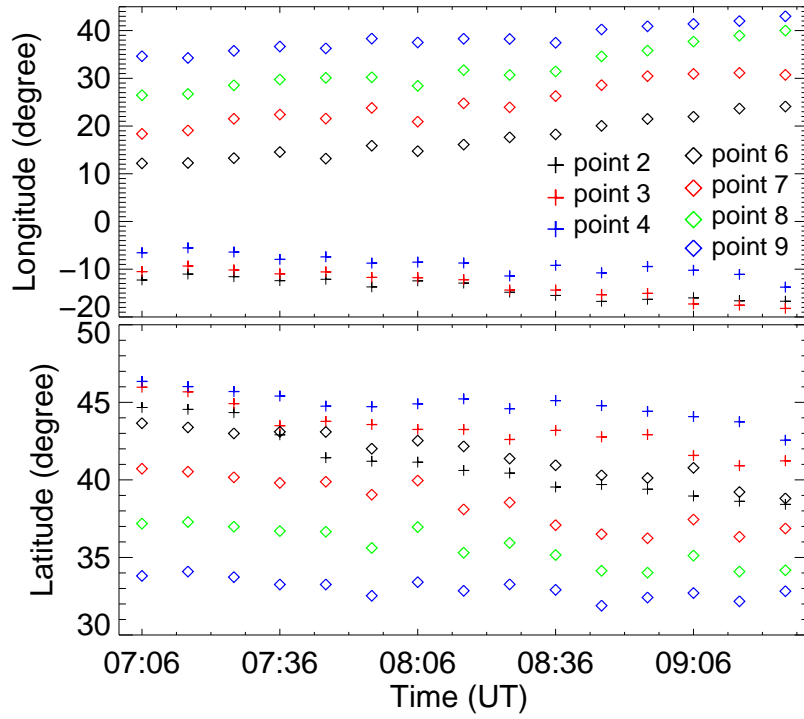
Fig. 8.— Longitude-time and latitude-time plots of different points of the filament. Points "2" to "4" are from the eastern leg, and points "6" to "9" are from the western leg (Figure 6).
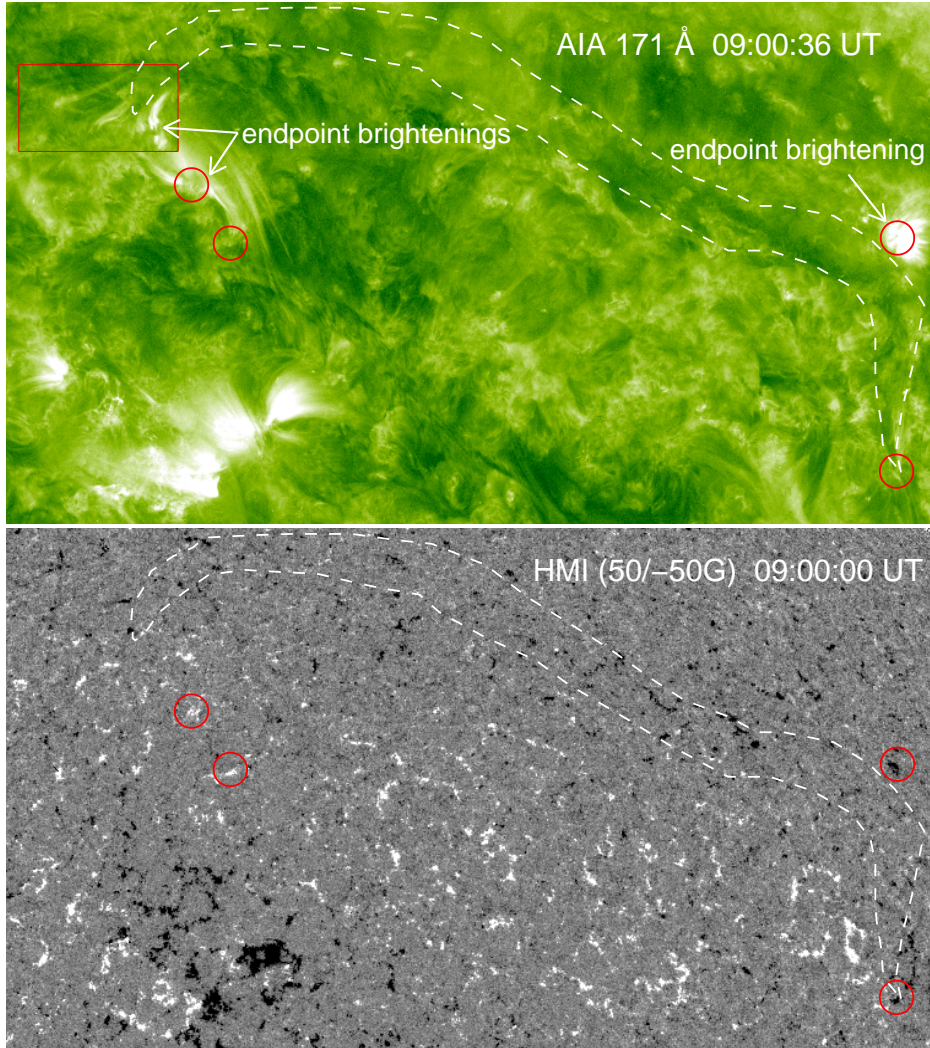
Fig. 9.— AIA 171 Å image (upper panel) and HMI line-of-sight magnetogram (lower panel) at the filament location. The white contours are the filament at 05:06 UT. The red circles denote the multiple endpoints of the filament. The red rectangle is the 171 Å image at 07:40 UT.
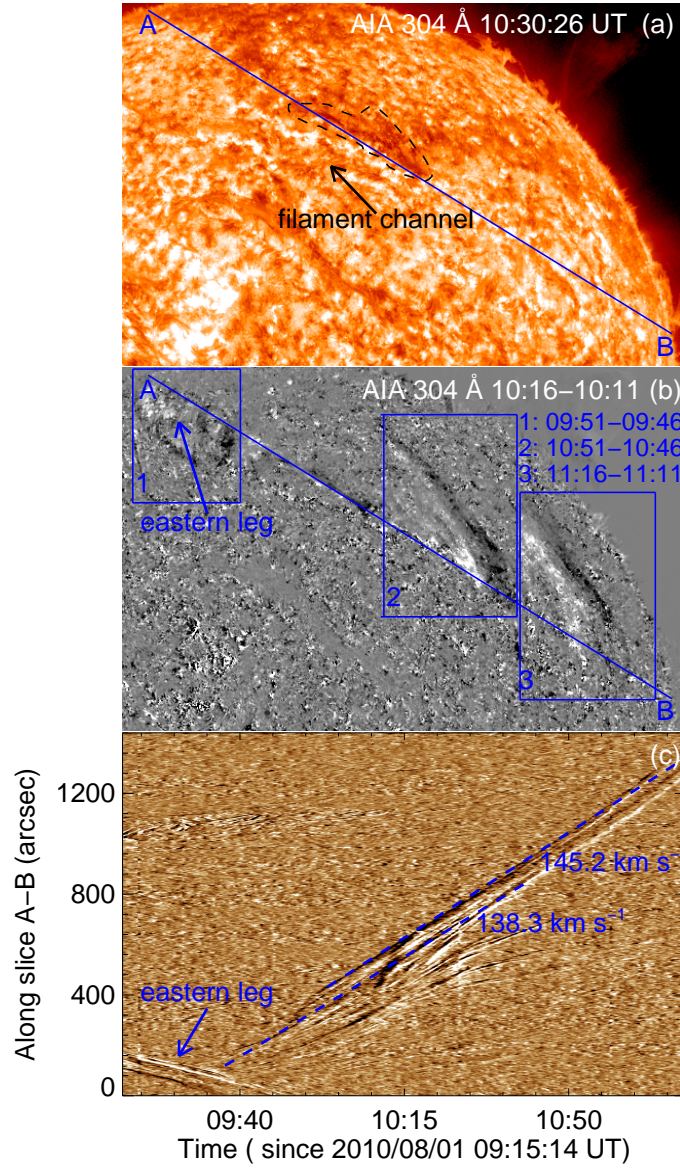
Fig. 10.— Appearance of the second eruption of filament material seen in AIA 304 Å (panel (a)) and running-difference images (panel (b)) and the running ratio stack plot obtained along slice A-B (panel (c)). The black contour denotes the filament material along line A-B.